HHS Public Access

Author manuscript

Arterioscler Thromb Vasc Biol. Author manuscript; available in PMC 2024 June 01.

Published in final edited form as:

Arterioscler Thromb Vasc Biol. 2023 June ; 43(6): 958–970. doi:10.1161/ATVBAHA.122.318938.

MRI of mouse cerebral cavernomas reveal differential lesion progression and variable permeability to gadolinium

Delaney G. Fisher[1,#], **Khadijeh A. Sharifi**[2,3,#], **E. Zeynep Ulutas**[4], **Jeyan S. Kumar**[3], **M. Yashar S. Kalani**[5], **G. Wilson Miller**[1,6], **Richard J. Price**[1], **Petr Tvrdik**[2,3]

[1]Department of Biomedical Engineering, University of Virginia, Charlottesville, VA

[2]Department of Neuroscience, University of Virginia, Charlottesville, VA

[3]Department of Neurosurgery, University of Virginia Health System, Charlottesville, VA

[4]Department of Neuroscience, Georgia Institute of Technology, Atlanta, GA

[5]St. John's Neuroscience Institute, Tulsa, OK

[6]Department of Radiology & Medical Imaging, University of Virginia, Charlottesville, VA

Abstract

BACKGROUND: Cerebral cavernous malformations (CCM), also known as cavernous angiomas, are blood vessel abnormalities comprised of clusters of grossly enlarged and hemorrhage-prone capillaries. The prevalence in the general population, including asymptomatic cases, is estimated to be 0.5%. Some patients develop severe symptoms, including seizures and focal neurologic deficits, while others remain asymptomatic. The causes of this remarkable presentation heterogeneity within a primarily monogenic disease remain poorly understood.

METHODS: We established a chronic mouse model of CCM, induced by postnatal ablation of *Krit1* with *Pdgfb-CreERT*, and examined lesion progression in these mice with T2-weighted 7T MRI. We also established a modified protocol for dynamic contrast-enhanced (DCE) MRI and produced quantitative maps of gadolinium tracer gadobenate dimeglumine. After terminal imaging, brain slices were stained with antibodies against microglia, astrocytes, and endothelial cells.

RESULTS: These mice develop CCM lesions gradually over 4–5 months of age throughout the brain. Precise volumetric analysis of individual lesions revealed non-monotonous behavior, with some lesions temporarily growing smaller. However, the cumulative lesional volume invariably increased over time, and after about 2 months followed a power trend. Using DCE MRI, we produced quantitative maps of gadolinium in the lesions, indicating a high degree of heterogeneity in lesional permeability. MRI properties of the lesions were correlated with cellular markers for

Correspondence to: G. Wilson Miller, PhD, Department of Radiology & Medical Imaging, University of Virginia, Charlottesville, VA. gwm2n@virginia.edu. Richard J. Price, PhD, Department of Biomedical Engineering, University of Virginia, Charlottesville, VA. rprice@virginia.edu. Petr Tvrdik, PhD, Department of Neurosurgery and Neuroscience, University of Virginia Health System, Charlottesville, VA. tvrdik@virginia.edu.

[#]D.G. Fisher and K.A. Sharifi share first authorship

Disclosures

The authors have no conflicts of interest to declare that are relevant to the content of this article.

endothelial cells, astrocytes, and microglia. Multivariate comparisons of MRI properties of the lesions with cellular markers for endothelial and glial cells revealed that increased cell density surrounding lesions correlates with stability, while denser vasculature within and surrounding the lesions may correlate with high permeability.

CONCLUSIONS: Our results lay a foundation for better understanding individual lesion properties and provide a comprehensive pre-clinical platform for testing new drug and gene therapies for controlling CCM.

Graphical Abstract

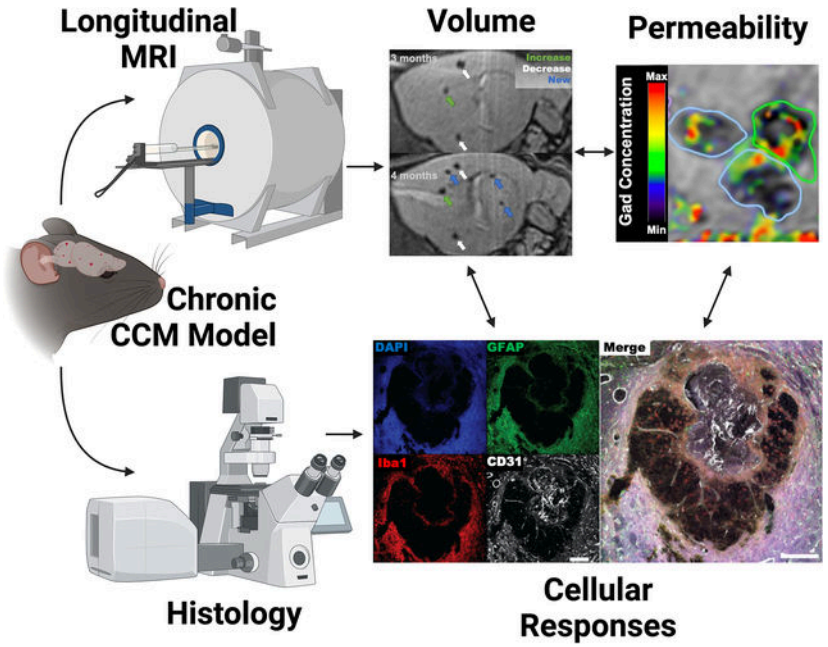

Introduction

Cerebral cavernous malformations (CCM), also referred to as cavernomas, are hemorrhage-prone, slow flow venous lesions that arise in the central nervous system and affect approximately 0.5% of the general population [1–3]. CCM form as a result of bi-allelic mutations in one of the three main causative genes—*KRIT1*, *CCM2*, or *PDCD10* [4]. Homozygous germline mutations are embryonic lethal in mice and, presumably, humans [5–7]. Heterozygous germline loss-of-function mutations show variable frequency in different human populations [8,9]. While usually asymptomatic outwardly, CCM have been associated with increased vascular permeability [10,11]. Further, the increased incidence of a second somatic mutation can drive the familial form of the disease, which presents with earlier disease onset and a higher lesion burden, compared to sporadic cases caused solely by biallelic somatic mutations [12,13].

One outstanding mystery regarding CCM is the diversity of patient symptom presentation and the degree of symptom severity [14–16]. Some patients with CCM can experience disabling symptoms that commonly include weakness, numbness, severe headaches, vision changes, and difficulty with language. More severe symptoms can include stroke, seizures,

and even paralysis. Meanwhile, other patients remain asymptomatic. Symptoms typically arise due to cavernomas that have hemorrhaged. However, the trajectory of clinical outcomes of lesions remains unpredictable. Many investigations have been conducted to better understand the heterogeneity of disease severity at the genetic level. For instance, it has recently been discovered that *PIK3CA* gain of function mutations can co-exist with CCM mutations within lesions and may be associated with more severe disease presentation [13,17,18]. Studies have been conducted to utilize MR scans of patients to correlate lesion stability (i.e. growth and hemorrhage risk) with MR-assessed features of permeability and susceptibility (iron deposition) [19–22]. While these studies show correlations of instability with lesion permeability and susceptibility, they fail to elucidate the molecular or cellular basis within and surrounding lesions that correspond with these MR features. Despite the extensive effort to develop predictive models [23,24], the variability in patient presentation remains to be wholly explained. Recommendation of clinical treatment cannot be fully informed without understanding of lesion trajectory.

Animal models of CCM that reflect the human pathology and patient heterogeneity are necessary for uncovering the heterogeneity seen in patients. Traditionally, acute animal models have been used for rapid screenings of pharmaceutical agents, but they lack many key features of the human pathology. Recently, strides have been made in developing chronic models of the disease that better encompass the human pathology. Cre-inducible models have proven useful for emulating loss of CCM gene heterozygosity in humans. Indeed, chronic models of *Pdcd10* and *Ccm2* mutations have recently been generated and characterized [25,26]. *Krit1* mutations are the most prevalent causation of the disease. However, chronic models of *Krit1* have had limited characterization and have been largely confined to postnatal tamoxifen induction at P1, restricting lesions to the cerebellum and retina [27,28].

Despite progress with these new models, most have yet to be robustly characterized with clinically relevant procedures. As MRI is a staple of CCM diagnosis and monitoring in patients, it is equally needed in pre-clinical studies for interpreting mechanistic investigations of CCMs in the context of human disease and for designing improved therapeutic interventions [29]. Prior to therapeutic intervention, it is imperative to understand the baseline progression of the disease without therapeutic intervention and to determine optimal timing of therapeutic intervention. Furthermore, MR sequences that can evaluate lesion permeability and hemosiderin deposition have been developed in patients with the goal of predicting stability of cavernomas in terms of their growth and hemorrhage [10,19,20,30]. Developing these MR sequences for mouse models of CCM would enable improved assessment of therapeutic intervention risk (i.e., acute hemorrhage due to therapy) and allow for longitudinal monitoring of therapeutic efficacy towards stabilizing the volume and bleeding of treated cavernomas. To this end, we have generated a chronic, tamoxifen inducible *Krit1* model with reduced tamoxifen dose and delayed induction that recapitulates the human CCM pathology. We then developed MRI protocols to enable longitudinal characterization of individual lesion progression throughout the whole brain in terms of lesion volume and permeability. We ensured that our MRI protocols align with immunohistochemical staining of lesions. Further, we identified relationships between our MRI-assessed features of lesions and cellular responses within and surrounding individual

lesions. Together, this study lays the foundation for better prognostication of CCM lesion behavior.

Materials and Methods

Raw MRI data have been made publicly available at Libra, the University of Virginia's scholarly institutional repository, and can be accessed at https://www.library.virginia.edu/libra. Matlab scripts and other data supporting the findings in this study are available from the corresponding authors upon reasonable request. The Supplemental Figures, Supplemental Tables, Legends for Supplemental Videos, and the Major Resources Table can be found in the Supplemental Material.

Animals and Treatments

All animal experiments were approved by the Animal Care and Use Committee at the University of Virginia. The animals were housed under standard laboratory conditions (22°C and 12h/12h light/dark cycle) and fed ad libitum Teklad 7912 chow (Irradiated LM-485 Mouse/Rat Sterilizable Diet from Harlan Laboratories, containing 19% crude protein, 5% crude fat, and 5% crude fiber). The breeder pairs had free access to Teklad 7904 (Irradiated S-2335 Mouse Breeder Diet, Harlan Laboratories, containing 17% crude protein, 11% crude fat, and 3.5 % crude fiber). All transgenic lines have been kept on a mixed C57BL/6J and 129/Sv genetic background. The *Pdgfb* $^{iCreERT2\text{-}IRES\text{-}EGFP}$ (*Pdgfb-CreERT*) line was described previously [31]. To generate experimental animals, male *Pdgfb-CreERT* mice were crossed to the floxed and null *Krit1* alleles (*Krit1*$^{fl/null}$) [28] to produce the desired genotype *Pdgfb-CreERT*; *Krit1* $^{fl/null}$ males or females. Genotyping was performed by Transnetyx (Cordova, TN) using real-time PCR assays specific for *Krit1* wt, floxed and null alleles, as well as the codon-improved Cre recombinase in *Pdgfb-CreERT. Krit1* gene ablation was induced with a single subcutaneous injection of 50uL of tamoxifen dissolved in corn oil at a concentration of 2 mg/mL between postnatal day 5 and 7. To induce inflammatory responses, 0.1 mg/mL solution of lipo-polysaccharides in PBS (LPS, Sigma-Aldrich L4391) was injected in 50 μL i.p., corresponding to 0.25 mg/kg dose, 12 h prior to imaging.

MR Imaging

A 7T small animal MRI scanner (Bruker/Siemens ClinScan) was used to acquire T2-SPACE, SWI and T1 contrast images. Mice were imaged monthly, starting as early as one month of age and as late as 5 months of age. To be included in this study, each animal had to have at least two imaging time points conducted. Three-dimensional T2-SPACE MRIs were acquired for all mice in this study using a repetition time of 3000 ms, echo time of 80 ms, pixel size of 125 μm × 125 μm × 100 μm, and 2 averages. Scan time for the T2-SPACE sequence was ~20 min. T1 contrast mapping was executed by performing 3D spoiled gradient echo sequences at various flip angles before, and 5 minutes after, gadolinium contrast injection, including the following flip angles: 1, 2, 4, 8, 12, 20, and 30°. All sequences in this series had a repetition time of 10 ms, echo time of 2.6 ms, pixel size of 187.5 μm × 187.5 μm × 200 μm, and 1 average. The scan time for the total image series (pre and post contrast injection combined) was ~20 minutes. To initially determine the optimal time to acquire the post-gadolinium image series such that gadolinium accumulation

is maximized and time is minimized, the post-series was repeated every 4 minutes following gadolinium injection up to 20 minutes (Figure S4). Gadolinium contrast (MultiHance) was injected as a bolus intravenously with a dose of 0.01 mmol diluted in saline at a molarity of 0.2mmol/mL.

Generation of Gadolinium Concentration Maps

Separate pre-contrast and post-contrast T1 maps were calculated from each series of multiple-flip-angle 3D images using standard methods [32]. Briefly, the MR signal magnitude as a function of flip angle θ_n was fit to the function

$$S_n = \frac{M_0 \sin\theta_n \left(1 - e^{-TR/T1}\right)}{1 - e^{-TR/T1}\cos\theta_n}$$

at each pixel containing nonzero signal, using the known value of the repetition time (TR = 10 ms) and sequence of flip angles $\theta_n = 1,\ 2,\ 4,\ 8,\ 12,\ 20,\ 30°$. Deposited gadolinium concentration was then calculated at each brain pixel from the measured pre/post T1 change, using the known relaxivity of MultiHance (R=6.3 L/mmol/s) in the expression:

$$C = \frac{1}{R\left(\frac{1}{T_{1,\ post}} - \frac{1}{T_{1,\ pre}}\right)}$$

Physically impossible concentration values (those that were larger than the initial gadolinium concentration in the blood or significantly less than zero, usually occurring in image regions with low SNR) were excluded from further analysis.

Segmentation of Lesions from MR Images

T2-SPACE images and gadolinium concentration maps were processed and analyzed in Horos DICOM viewer. T2-SPACE and gadolinium concentration maps were co-registered with the built-in feature within Horos or manually with custom MATLAB script. Manual segmentation of lesions were made with the freehand tool by outlining lesions in every coronal slice for each mouse and imaging timepoint within the study. Lesion volumes were calculated with the Horos “Compute Volume” feature and recorded. ROIs from T2-SPACE images were transposed onto co-registered gadolinium concentration maps. Total grayscale value within ROIs were recorded and summed across all slices for a given lesion (equivalent to gadolinium mass). Gadolinium concentration was calculated by dividing total gadolinium mass by computed lesion volume. Individual lesions were manually tracked across imaging time points using T2-SPACE images. The same anatomical location of a tracked lesion was validated in each imaging plane (coronal, axial, sagittal) across imaging timepoints. In some instances, distinct lesions from earlier time points had merged into one lesion at later time points. In other cases, lesions from earlier time points were no longer visible on images from later time points. De novo lesion formation was found in all animals in our study. If a lesion was obscured due to an imaging-related artifact, the lesion was excluded from analysis at the corresponding timepoint.

Histology

After completion of the final imaging timepoint, mice were transcardially perfused with phosphate-buffered saline (PBS) and 4% PBS-buffered formaldehyde (EMS 15714). Brains were dissected, post-fixed, sequentially equilibrated in 10% and 30% sucrose and embedded in OCT (Andwin Scientific). Frozen brains were cryosectioned at 50- to 80-μm thickness for histology staining, or 25-μm thickness for immunohistochemistry (IHC). To perform histological staining of neurons and blood vessels in 50-μm thick sections, free floating sections were permeabilized overnight in PBS-buffered 0.5% Triton X-100 (Sigma-Aldrich 93443) at 4°C. Next, the sections were washed 3 times for 5 min with PBS, 1 mM $CaCl_2$, and incubated in the red fluorescent Nissl stain (Neurotrace, Invitrogen N21482, diluted 1:100 in PBS, 1mM $CaCl_2$) for 2 h at room temperature (RT). Following three washes with PBS, 1mM $CaCl_2$, the sections were stained with Alexa Fluor 488-conjugated Isolectin GS-IB4 (Invitrogen 121411, diluted 1:100 in PBS, 1mM $CaCl_2$) overnight at 4°C. After one final wash with PBS, 1mM $CaCl_2$, the sections were mounted on microscopy slides with DAPI Fluoromount-G (SouthernBiotech, 0100–20) using Secure Seal Spacers (EMS 70327–20S).

Immunohistochemistry

Thawed 25-μm sections were rehydrated with PBS, permeabilized in 0.5% Triton X-100 (Sigma-Aldrich 93443) in PBS for 1h at RT, and blocked with 1% bovine serum albumin (BSA, Jackson ImmunoResearch Labs, 001–000-161), 5% normal donkey serum (NDS, Jackson ImmunoResearch Labs, 017–000-121), and 0.5% Triton X-100 in PBS for 2 h at RT. The primary antibodies, including chicken anti-GFAP (1:200, Aves, GFAP5727980), rabbit anti-Iba1 (1:500, Wako Chemicals USA, 011–27991), goat anti-CD31 (1:20, R&D Systems, AF3628), were diluted in the blocking solution and incubated with mounted brain sections overnight at 4°C. After three 5-min washes with PBS, 0.5% Triton X-100, the sections were incubated with secondary antibodies, including donkey anti-chicken Alexa 488 (1:500, Jackson ImmunoResearch Labs, 703–546-155), donkey anti-rabbit Alexa 568 (1:500, Invitrogen A10042), donkey anti-goat Alexa 647 (1:500, Invitrogen A21447), diluted in the blocking solution at 1:500 for 2 h at RT. Following final washes, slides were mounted with ProLong Gold antifade reagent with DAPI (Invitrogen, P36935) and cover slipped with Fisherbrand Microscope Cover Glass (12–544-E) for confocal imaging.

Confocal Microscopy

Stained sections were imaged with a Zeiss LSM 880 confocal microscope (Zeiss, Germany) using sequential scanning mode for DAPI, Alexa 488, 568 and 647 dyes. Montages of image stacks (1024 × 1024 pixels, 2 μm z-step), tiled in the x-y plane, were processed with Imaris 9.9 (Oxford Instruments) and analyzed with Fiji/ImageJ. Final images were adjusted with Adobe Photoshop and assembled in PowerPoint (Microsoft), or Adobe Illustrator (Adobe Creative Cloud).

Segmentation of Lesions from IHC Images

Fluorescent images were analyzed in ImageJ for grayscale intensities in each channel: Iba1, GFAP, CD31, and DAPI. ROIs of lesion boundaries were manually drawn around the central

hypointense void space of each identified lesion (enlarged vessels near the lesion were not included for this ROI). To measure cell populations surrounding the lesions, this lesion boundary was expanded by either 50 μm or 100 μm, and the inside ROI was subtracted. Mean grayscale intensity of each of the three ROIs (inside lesion, 50 μm border, and 100 μm border) was averaged for all slices within the image stack in a given channel. Mean grayscale intensity for three reference ROIs drawn in nearby non-lesional locations of the brain tissue in each image were also averaged across the image stack in a given channel. Lesion associated mean grayscale intensities were normalized to the average reference mean grayscale intensity in the same image to account for variations of cell population expression in differing brain regions. These normalized mean grayscale intensities for Iba1, GFAP, CD31, and DAPI for each lesion were correlated with the same lesion's volume and gadolinium concentration from the last imaging timepoint. Spearman's correlation analysis was then performed with OriginPro's Correlation Plot on the data matrix for 17 lesions and 14 measurements (3 lesion boundaries × 4 channels + lesion volume + lesion gadolinium concentration).

Statistical analysis

The results were expressed as means ± standard error of the mean (SEM). In all experiments, the statistical significance was set at $P < 0.05$. One-way repeated measures ANOVA, and mixed-effects model with repeated measures and Tukey's correction was performed using GraphPad Prism 8 statistical package software (San Diego, USA). Linear regression was calculated on the original scales for gadolinium concentration and lesion volume (GraphPad Prism 8). Spearman Rank correlation coefficient and Principal component analysis (PCA) calculations were performed with Origin Pro 2020 (OriginLab Corporation). In all Figures, the legends include "n" values indicating biological replicates, and data attributed to individual mice are color-coded with the same color scheme throughout the paper. The number of biological replicates for each individual time point are stated in the text when referring to the corresponding Figure. To improve power, data from male and female mice were combined. Sample size did not allow for a statistical determination of sex interaction within this study. Sex of mice is indicated in Figure panels as well as in Figure legends whenever data are disaggregated to individual animals.

Results

Delayed postnatal deletion of *Krit1* in the *Pdgfb* domain generates a chronic CCM model with multiple lesions distributed throughout the brain

To study CCM lesion properties in the adult mouse brain, we developed a genetic strategy that gradually generates cavernomas throughout the entire brain over the young adult life span. Traditionally, tamoxifen-induced deletion of conditional CCM alleles was initiated soon after birth (postnatal days P1-P3). However, this early timing severely affects the rapidly developing murine cerebellum, leading to the formation of multiple hemorrhage-prone lesions and a high mortality around one month of age. Delaying the timing of tamoxifen injection to later stages of angiogenic development (P6-P8) was previously found to reduce the lesion burden in the *Pdcd10* model of CCM [26]. We have therefore delayed CCM gene ablation to P5-P7. In our approach, we crossed the males of the *Pdgfb*

iCreERT2-IRES-EGFP strain [31] (hereafter *Pdgfb-CreERT*) with females harboring the floxed *Krit1* allele [28]. The *Pdgfb-CreERT* studs also carried the null (germline-excised) *Krit1* allele (*Krit1* $^{fl/null}$), emulating familial inheritance pattern of the disease. Only heterozygous progeny of the *Pdgfb-CreERT*; *Krit1* $^{fl/null}$ genotype were used. A single injection of dilute tamoxifen in the dorsal subcutaneous region reliably induced lesion formation beginning at 1 month of age and extending through young adult life (4–5 months; Figure 1A). Lesions form throughout the whole brain; frequently in the periventricular striatum and along the hippocampal folds, but are also regularly found in the cerebellum, olfactory bulb, thalamus, cerebral cortex and brainstem (Figure 1B, Figure S1). Most mice of this model appear grossly similar to their littermate controls; however, some mutants developed anal prolapse or hydrocephalus. We used a T2-weighted MRI sequence, described below, to detect lesions in live animals. We confirmed that hypo-intensities detected with T2 MRI *in vivo* can be unequivocally matched with vascular lesions identified in brain cryosections from these animals with isolectin IB4 (Figure 1C), establishing a robust correlation between MRI and histology. Thus, delayed ablation of *Krit1* generates CCM lesions over time throughout the brain and these lesions can be readily identified with MR imaging, and cross-examined with histology and immunohistochemistry.

Longitudinal MRI demonstrates dramatic increases in individual lesion size and total lesion burden with age

We systematically measured lesion burden in the CCM mice using a three-dimensional T2-weighted isotropic fast spin-echo MRI sequence (T2-SPACE), which enables 3D image acquisition with a high resolution and relatively short scan times [33–35]. Traditional sequences for CCM detection, such as T2*-weighted gradient echo and susceptibility weighted imaging (SWI), have an increased sensitivity to lesions but come at the cost of an enlarged distortion of cavernoma size due to volume averaging and poor spatial resolution. We therefore employed the T2-SPACE sequence at 7T magnetic strength, as previously optimized for the ClinScan MRI Animal Scanner (Bruker Corporation) used in this study. In line with published literature, T2-SPACE robustly delineated the lesion dimensions as well as internal architecture [36,37].

We used longitudinal T2-SPACE on 9 mice from 5 distinct litters at 5 time points: At 1 month of age (n=3 from 2 litters), 2 months (n=7 from 4 litters), 3 months (n=3 from 2 litters), 4 months (n=5 from 4 litters), and 5 months (n=1; Figure 2). This imaging revealed that CCM formation began with low numbers at 1 month of age, and progressed with age throughout the entire brain. We tracked the lesion volume for each mouse over time, as illustrated in Video S1. Next, we plotted the cumulative lesion load for each animal at each age-point (Figure 2B). The median total lesion volume in the brain was 0.041 mm^3 at 1 month of age, 0.044 mm^3 at 2 months, 0.714 mm^3 at 3 months, 18.486 mm^3 at 4 months, and 46.721 mm^3 at 5 months. Correlation analysis revealed that cumulative lesion load showed a significantly increasing trend with age, with slope=0.976±0.011 SEM ($p<0.001$, random coefficient regression analysis of $\log_{10}$ transformed lesion volume [mm^3] onto mouse age) (Figure 2B, Table S1). This analysis indicated that the total lesion volume grew approximately 10-fold per month in 2–4-month-old mice. T2-SPACE images of each mouse were then analyzed to track individual lesions across imaging timepoints. This individual

lesion analysis revealed that lesions in every mouse displayed variable growth rates, including negative rates (i.e. shrinkage of lesion size; Figure 2C). However, the majority of individual lesions increased in size with age. The number of small lesions (0.01 to 0.1 mm^3) significantly increased every month between ages 1–4 months; and the number of intermediate lesions (0.1 to 1 mm^3) at 4 months was significantly greater than previous age points (Figure S2). Altogether, our chronic *Krit1* CCM mouse model displays progressive lesion formation and increasing cumulative lesion burden with age, which is seen in patients with familial CCM [14,38,39]. These results indicate that our model is well-suited for studying individual and variable lesion dynamics with context relevant to the human pathology. Of note, susceptibility-weighted imaging (SWI) MRI sequences are also used due to their increased sensitivity to inhomogeneities in magnetic field strength surrounding iron-rich lesions. This sequence often produces what is called a “blooming” artifact [40,41]. We tested a SWI sequence optimized for the 7T ClinScan MRI scanner and imaged CCM animals immediately prior and after acute LPS-mediated inflammation. This approach demonstrated a greater sensitivity to post-infection lesion increases due to presumed bleeding (Figure S3). However, this increased sensitivity to susceptibility effects also enlarges lesions in the produced image by distorting their perceived size as previously described [42,43], disqualifying this approach from accurate volumetric assessment of CCM lesions.

T1 Contrast Maps of MultiHance deposition reveal individual lesion permeability

We next sought to characterize the lesion “leakiness”, or internal permeability, with MultiHance (gadobenate dimeglumine), a ~1 kDa MRI gadolinium-based contrast agent. We used a modified version of dynamic contrast enhanced (DCE) MRI [44] that we have termed T1 contrast mapping, as described in the Methods and Figure S4. Briefly, T1 maps were constructed from MR images acquired from CCM mice prior to and following a MultiHance bolus injection. The T1 changes due to contrast accumulation were used to determine local concentrations of the contrast agent. In practice, the total deposition of gadolinium serves as a measurement of lesion leakiness, which lends insight into the potential hemorrhage risk of a lesion and its clinical instability. Compared to traditional DCE methods, which provide temporal information about gadolinium accumulation but are typically confined to a few MR slices of the brain [45], our T1 contrast mapping approach enables whole brain analysis of lesion permeability.

We employed longitudinal T1 contrast mapping on 6 of the 9 mice that received volumetric image analysis. A dataset was acquired for ages of 1 month (n=1), 2 months (n=4 from 3 litters), 3 months (n=2 from 1 litter), 4 months (n=3 from 3 litters), and 5 months (n=1; Figure 3). T1 mapping generated gadolinium concentration maps that were registered with T2-SPACE sequences, enabling us to quantify gadolinium deposition in T2-SPACE-defined lesions (Figure 3A; Video S2 and S3). We plotted the total lesional gadolinium deposition for each mouse over time and found that cumulative lesion leakiness increased with age (Figure 3B). Median total gadolinium deposition was 0.476 μg at 1 month of age, 0.504 μg at 2 months, 3.08 μg at 3 months, 5.48 μg at 4 months, and 12.5 μg at 5 months. Regression analysis showed a significant positive trend over time, following a slope of 0.398±0.089 SEM (p=0.004, random coefficient regression analysis of $\log_{10}$ transformed gadolinium mass [pg] onto mouse age) (Figure 3B, Table S2), supporting

the notion that total gadolinium deposition in the lesions increased approximately 2.5-fold per month in 2–4-month-old animals. The gadolinium concentration maps of each mouse were then analyzed to track individual lesions across imaging time points. This individual lesion analysis revealed that many T1-mapped lesions displayed variations in gadolinium deposition over time, with several lesions displaying decreased gadolinium deposition at follow-up measurements (Figure 3C). However, most individually tracked lesions increased in gadolinium deposition with age. Specifically, the total number of lesions in the 10^4 to 10^5 pg/mm^3 gadolinium concentration range significantly increased in 4-month-old mice compared with 2-month-old animals (Figure S5). Taken together, our data shows that the chronic *Krit1* CCM mouse model is characterized by progressive lesion burden with cumulative increases in lesion number, volume, and leakiness with age. Individual lesions can demonstrate variable changes in size and leakiness, which has also been in seen in human patients [10,30,46–48].

CCM lesion permeability is highly variable and correlates poorly with lesion volume

We asked if any correlation existed between lesion volume and lesion leakiness. The total gadolinium deposition in individual lesions was scaled by lesion volume to produce specific gadolinium concentration. Gadolinium concentrations in individual lesions were then plotted against the lesion volume for each imaging point. Concentration versus volume plots were generated for 1 month of age (n=1), 2 months (n=4 from 3 litters), 3 months (n=2 from 1 litter), 4 months (n=3 from 3 litters), and 5 months (n=1; Figure 4). A linear regression fitted to these plots revealed no correlation between lesion volume and gadolinium concentration in our measurements. The coefficient of determination (R^2) values were considerably low (ranging from 0.001 to 0.053, Figure 4) at all age points, suggesting a poor linear relationship. In other words, our analysis reveals a high degree of heterogeneity of lesion permeability between individual animals, and over their lifespan. This heterogeneity was also observed in lesions within individual mice harboring a sufficient number of datapoints (Figure S5 and S6). It is noteworthy that heterogeneity of individual lesion permeability was also observed in human patients using similar MR techniques [10,30]. Thus, our mouse model of CCM appears to recapitulate the heterogenous lesion permeability properties seen in human CCM patients.

Increased gadolinium deposition in the lesions correlates with decreased cell density in the surrounding parenchyma

Lastly, we asked if the MRI features identified in CCM lesions, namely the lesion volume and lesion permeability, correlated with histological features in close proximity of the lesions. For this analysis, we entirely sectioned the L9-M3 brain and stained with antibodies directed against Iba1 (for microglia), GFAP (for astrocytes) and CD31 (aka PECAM-1, for endothelial cells). The nuclear stain DAPI was included in the mounting media. In total, we identified 17 lesions in confocal montages of the coronal sections that were unequivocally matched with the T2-SPACE MRI sequence recorded immediately prior to brain extraction. High resolution images of the lesions were then used to measure fluorescence signal mean intensity of these three cell populations within the lesion, within the 50-μm perimeter of the lesion, as well as within the 100-μm perimeter of the lesion (Figure 5, Figure S7, Table S3). The specific cell type intensities were then correlated to lesion volume and gadolinium

concentration using the non-parametric Spearman's rank correlation test. Correlation analysis revealed that both the 50 μm and 100 μm perimeters for each cell population showed the same correlation direction, and thus, the two perimeters are sometimes jointly referred to as 'outside of the lesion'. Specifically, this analysis revealed that cell density outside the lesions, determined as DNA content by DAPI fluorescence within the immediate 50-μm perimeter of the lesion, was inversely correlated with gadolinium concentration inside the lesion ($r = -0.61$; $p < 0.01$). The 100-μm ring was also inversely correlated, although at a lower significance level ($r = -0.51$; $p < 0.05$) (Figure S8 and S9). Principal component analysis (PCA) corroborated inverse correlation between gadolinium and DAPI, along with weaker trends towards inverse correlations of gadolinium with microglial and astrocytic densities outside the leaky lesions (Figure S10). Conversely, the glial density inside the lesion correlated positively, albeit weakly, with gadolinium concentration. The endothelial cell density both inside and outside the lesion showed weak positive correlations with gadolinium concentration. On the other hand, lesion volume did not correlate with gadolinium deposition ($r = -0.14$, $p = 0.58$), in line with previous measurements. Of other noticeable trends, microglia and astrocytes both inside and outside the lesions appear to be inversely correlated with lesion volume, whereas endothelial cells both inside and outside of lesions trended positively with lesion volume (Figure S9 and S10).

Our data points to a relationship between high lesion permeability and glial cell density. This data may suggest that dense vascularization, both inside and outside of the lesions, may have negative effects on lesion stability. Conversely, this data could also suggest that lesion instability drives the production of vasculature inside and outside the lesion.

Discussion

Despite years of investigation, it is still poorly understood why CCM patients have heterogenous presentation in symptoms and lesion phenotypes. Due to the difficulties associated with human studies and limited access to human tissue samples, generation of animal models that reliably capture the human pathology are necessary for studying and furthering treatment of this disease. In this manuscript, we describe a chronic *Krit1* CCM model with delayed tamoxifen induction that replicates human features of lesion development throughout the whole brain and resembles lesion dynamics found in human patients. We also characterize, for the first time, individual CCM lesion progression through the combination of multiple clinical MRI sequences performed longitudinally and immunohistochemical staining of cell populations. This unique merging of a clinically relevant mouse model with advanced MR imaging tools represents a powerful new platform for testing mechanisms of CCM disease, as well as for identifying and pre-clinically testing promising new therapies.

Following generation of our model, we employed clinically relevant MRI sequences longitudinally to characterize lesion progression and dynamics. MRI is commonly used to diagnose and monitor CCM in patients. Despite its ubiquity in the clinic, MR imaging has been largely neglected in many pre-clinical studies, with little data existing on MRI-based longitudinal characterization of mouse cavernoma. Using T2-SPACE to accurately assess lesion volume and T1 contrast mapping to assess lesion "leakiness," we find that lesion

volume and permeability cumulatively increase with age, while the rates of growth and leakiness can be variable across individual lesions over time. Notably, this variability in lesion growth rate and permeability has also been shown in patients [10,30,46–48]. Our results differ from that in Mikati et al. where patients with familial CCM were shown to not have a correlation between permeability and age [10]. However, due to the restriction of their DCEQP protocol (which is confined to 4–6 MRI slices) only a limited number of lesions could be tracked in individuals, whereas our T1 contrast mapping protocol allows for whole brain assessment of lesion leakiness. Thus, we believe that lesion permeability is likely correlated with age for the familial disease if all lesions were examined [10]. Importantly, the development and translation of clinical MRI protocols for mouse models of CCM has allowed us to establish the baseline progression of the disease, which will be necessary for testing therapeutic approaches in the next phase.

To further understand lesion heterogeneity in our model, we sought to associate our MR features of lesion volume and lesion leakiness with cellular responses within and around lesions. A limited number of lesions have been correlated from MRI and H&E staining previously [49], but this is the first association of MRI and specific cell population markers to our knowledge. Spearman non-parametric correlation of our MR features and cell population markers suggested that more permeable lesions contain greater endothelial cell populations within and around cavernomas than less permeable lesions. Meanwhile, less permeable lesions trend toward higher astrocyte and microglial populations surrounding cavernomas than more permeable lesions.

The findings of this study have to be seen in light of some limitations. First of all, the development of a chronic CCM model with *Krit1* mutations was done in the absence of preexisting information on the lifespan of these mutants. Consequently, some of the observations in this work were affected by lack of statistical power due to diminishing size of the cohorts. Specifically, only one animal was imaged with MRI at 5 months after birth, and the comprehensive analysis correlating MRI and histological profiles was successfully completed in a single animal. In future experiments, the high mortality rate can be mitigated by reducing the *Krit1* gene ablation with a lower dose of tamoxifen, or by using the brain endothelial cell-selective Cre driver *Slco1c1-CreERT*[50]. In fact, a significant cause of health decline in our aging *Krit1* colony were gastrointestinal comorbidities such as rectal prolapse.

Next, our work takes the first step towards correlative analysis of MRI measurements of lesion permeability with molecular profiles in the mouse models of CCM. While performed in one representative animal, the extensive and evenly distributed lesion load in this specimen allowed appropriate statistical analysis. We found that the density of nuclear stain DAPI immediately outside the lesions correlated significantly and inversely with gadolinium deposition in the lesions, possibly combining the decreases in GFAP- and Iba1-staining that also trended similarly. Our findings that GFAP-positive astrocytes are less abundant around highly permeable lesions is different from the observations of Lopez-Ramirez at al., who recently postulated that astrocytes drive neurovascular dysfunction in the disease [51]. These differences could be ascribed to changing dynamics at different stages of this cellular interaction. Further, it should be noted that cell and vascular density varies greatly in various brain locations, which could have also affected the assessments of cell

density surrounding lesions. More multifaceted research is warranted to better elucidate the molecular underpinnings of CCM formation and stability.

Finally, while we have advanced MRI approaches to the mouse CCM model, more work is needed to strengthen pre-clinical MRI applications for cavernoma dynamics. It will be important to characterize if high gadolinium content inside the lesion correlates positively with gadolinium leakage in the surrounding brain parenchyma, which is clinically more relevant. It is also highly desirable to develop new sensitive MRI sequences for quantitative susceptibility measurements (QSM) suitable for high magnetic fields, which will enable more sensitive drug testing in the animals, especially in combination with more high-throughput approaches using automated segmentation algorithms. A robust dynamic contrast enhanced MRI method also remains a challenge in the mouse model, which would enable measurements of permeability rates within cavernomas. The development of these MRI techniques will be a continual focus for our group moving forward, enhancing pre-clinical CCM research to better inform clinical practice.

Conclusion

Chronic animal models of CCM are generated to test new therapeutic approaches that can be ultimately translated to the clinic. It is imperative that the models' representation of human pathogenesis is validated. To characterize and validate our CCM model, we optimized and utilized several clinically relevant MRI protocols. We show that key characteristics of the human pathology are recapitulated in our chronic model of CCM, including progressive lesion formation throughout the whole brain that increases with age, changes in size and leakiness of individual lesions over time, and heterogenous permeability of individual lesions. We next used the lesion MRI properties (such as lesion volume and leakiness) to stratify the lesions, and gain insight to the cellular composition within and surrounding lesions. We find that increased glial cell density surrounding the lesions is correlated with lesion stability, while increases in endothelial cells within and surrounding lesions may correlate with lesion instability. This study is the first to establish the baseline assessment of individual lesions in a chronic *Krit1* CCM murine model, providing a useful platform to advance novel treatment strategies for this debilitating disease.

Supplementary Material

Refer to Web version on PubMed Central for supplementary material.

Acknowledgments

We thank Dr. Kevin Whitehead for kindly providing the mouse strains used in this study. We are also grateful to Rene Jack Roy of the University of Virginia Molecular Imaging Core and Jeremy Gatesman of the University of Virginia Center for Comparative Medicine for assistance with MRI imaging and catheterization procedures, respectively. We acknowledge James Patrie, University of Virginia Health System, for his advice on statistical analysis. We also thank Dr. Ryan Kellogg for critically reading the manuscript.

Sources of Funding

This work was supported by funding from NIH R21NS116431 and grants from the Focused Ultrasound Foundation (FUSF), the Be Brave For Life Foundation, and the Alliance to Cure Cavernous Malformation to P. Tvrdik; NIH

R01EB030409, R01EB030744, and R21NS118278 to R.J. Price; NIH R01CA226899 to G.W. Miller, and AHA 830909 to D.G. Fisher.

References

1. Al-Holou WN, O'Lynnger TM, Pandey AS, Gemmete JJ, Thompson BG, Muraszko KM, Garton HJ, Maher CO. Natural history and imaging prevalence of cavernous malformations in children and young adults. J Neurosurg Pediatr. 2012;9:198–205. doi: 10.3171/2011.11.PEDS11390 [PubMed: 22295927]
2. Ene C, Kaul A, Kim L. Natural history of cerebral cavernous malformations. Handb Clin Neurol. 2017;143:227–232. doi: 10.1016/B978-0-444-63640-9.00021-7 [PubMed: 28552144]
3. Vernooij MW, Ikram MA, Tanghe HL, Vincent AJ, Hofman A, Krestin GP, Niessen WJ, Breteler MM, van der Lugt A. Incidental findings on brain MRI in the general population. N Engl J Med. 2007;357:1821–1828. doi: 10.1056/NEJMoa070972 [PubMed: 17978290]
4. Snellings DA, Hong CC, Ren AA, Lopez-Ramirez MA, Girard R, Srinath A, Marchuk DA, Ginsberg MH, Awad IA, Kahn ML. Cerebral Cavernous Malformation: From Mechanism to Therapy. Circ Res. 2021;129:195–215. doi: 10.1161/CIRCRESAHA.121.318174 [PubMed: 34166073]
5. Chan AC, Drakos SG, Ruiz OE, Smith AC, Gibson CC, Ling J, Passi SF, Stratman AN, Sacharidou A, Revelo MP, et al. Mutations in 2 distinct genetic pathways result in cerebral cavernous malformations in mice. J Clin Invest. 2011;121:1871–1881. doi: 10.1172/JCI44393 [PubMed: 21490399]
6. Kleaveland B, Zheng X, Liu JJ, Blum Y, Tung JJ, Zou Z, Sweeney SM, Chen M, Guo L, Lu MM, et al. Regulation of cardiovascular development and integrity by the heart of glass-cerebral cavernous malformation protein pathway. Nat Med. 2009;15:169–176. doi: 10.1038/nm.1918 [PubMed: 19151727]
7. Whitehead KJ, Plummer NW, Adams JA, Marchuk DA, Li DY. Ccm1 is required for arterial morphogenesis: implications for the etiology of human cavernous malformations. Development. 2004;131:1437–1448. doi: 10.1242/dev.01036 [PubMed: 14993192]
8. Akers A, Al-Shahi Salman R, I AA, Dahlem K, Flemming K, Hart B, Kim H, Jusue-Torres I, Kondziolka D, Lee C, et al. Synopsis of Guidelines for the Clinical Management of Cerebral Cavernous Malformations: Consensus Recommendations Based on Systematic Literature Review by the Angioma Alliance Scientific Advisory Board Clinical Experts Panel. Neurosurgery. 2017;80:665–680. doi: 10.1093/neuros/nyx091 [PubMed: 28387823]
9. Gunel M, Awad IA, Finberg K, Anson JA, Steinberg GK, Batjer HH, Kopitnik TA, Morrison L, Giannotta SL, Nelson-Williams C, et al. A founder mutation as a cause of cerebral cavernous malformation in Hispanic Americans. N Engl J Med. 1996;334:946–951. doi: 10.1056/NEJM199604113341503 [PubMed: 8596595]
10. Mikati AG, Khanna O, Zhang L, Girard R, Shenkar R, Guo X, Shah A, Larsson HB, Tan H, Li L, et al. Vascular permeability in cerebral cavernous malformations. J Cereb Blood Flow Metab. 2015;35:1632–1639. doi: 10.1038/jcbfm.2015.98 [PubMed: 25966944]
11. Yadla S, Jabbour PM, Shenkar R, Shi C, Campbell PG, Awad IA. Cerebral cavernous malformations as a disease of vascular permeability: from bench to bedside with caution. Neurosurg Focus. 2010;29:E4. doi: 10.3171/2010.5.FOCUS10121
12. McDonald DA, Shi C, Shenkar R, Gallione CJ, Akers AL, Li S, De Castro N, Berg MJ, Corcoran DL, Awad IA, et al. Lesions from patients with sporadic cerebral cavernous malformations harbor somatic mutations in the CCM genes: evidence for a common biochemical pathway for CCM pathogenesis. Hum Mol Genet. 2014;23:4357–4370. doi: 10.1093/hmg/ddu153 [PubMed: 24698976]
13. Ren AA, Snellings DA, Su YS, Hong CC, Castro M, Tang AT, Detter MR, Hobson N, Girard R, Romanos S, et al. PIK3CA and CCM mutations fuel cavernomas through a cancer-like mechanism. Nature. 2021;594:271–276. doi: 10.1038/s41586-021-03562-8 [PubMed: 33910229]
14. Denier C, Labauge P, Brunereau L, Cave-Riant F, Marchelli F, Arnoult M, Cecillon M, Maciazek J, Joutel A, Tournier-Lasserve E, et al. Clinical features of cerebral cavernous malformations

patients with KRIT1 mutations. Ann Neurol. 2004;55:213–220. doi: 10.1002/ana.10804 [PubMed: 14755725]

15. Gault J, Sain S, Hu LJ, Awad IA. Spectrum of genotype and clinical manifestations in cerebral cavernous malformations. Neurosurgery. 2006;59:1278–1284; discussion 1284–1275. doi: 10.1227/01.NEU.0000249188.38409.03 [PubMed: 17277691]
16. Gianfrancesco F, Cannella M, Martino T, Maglione V, Esposito T, Innocenzi G, Vitale E, Liquori CL, Marchuk DA, Squitieri F. Highly variable penetrance in subjects affected with cavernous cerebral angiomas (CCM) carrying novel CCM1 and CCM2 mutations. Am J Med Genet B Neuropsychiatr Genet. 2007;144B:691–695. doi: 10.1002/ajmg.b.30381 [PubMed: 17440989]
17. Hong T, Xiao X, Ren J, Cui B, Zong Y, Zou J, Kou Z, Jiang N, Meng G, Zeng G, et al. Somatic MAP3K3 and PIK3CA mutations in sporadic cerebral and spinal cord cavernous malformations. Brain. 2021;144:2648–2658. doi: 10.1093/brain/awab117 [PubMed: 33729480]
18. Weng J, Yang Y, Song D, Huo R, Li H, Chen Y, Nam Y, Zhou Q, Jiao Y, Fu W, et al. Somatic MAP3K3 mutation defines a subclass of cerebral cavernous malformation. Am J Hum Genet. 2021;108:942–950. doi: 10.1016/j.ajhg.2021.04.005 [PubMed: 33891857]
19. Girard R, Fam MD, Zeineddine HA, Tan H, Mikati AG, Shi C, Jesselson M, Shenkar R, Wu M, Cao Y, et al. Vascular permeability and iron deposition biomarkers in longitudinal follow-up of cerebral cavernous malformations. J Neurosurg. 2017;127:102–110. doi: 10.3171/2016.5.JNS16687 [PubMed: 27494817]
20. Mikati AG, Tan H, Shenkar R, Li L, Zhang L, Guo X, Larsson HB, Shi C, Liu T, Wang Y, et al. Dynamic permeability and quantitative susceptibility: related imaging biomarkers in cerebral cavernous malformations. Stroke. 2014;45:598–601. doi: 10.1161/STROKEAHA.113.003548 [PubMed: 24302484]
21. Tan H, Zhang L, Mikati AG, Girard R, Khanna O, Fam MD, Liu T, Wang Y, Edelman RR, Christoforidis G, et al. Quantitative Susceptibility Mapping in Cerebral Cavernous Malformations: Clinical Correlations. AJNR Am J Neuroradiol. 2016;37:1209–1215. doi: 10.3174/ajnr.A4724 [PubMed: 26965464]
22. Zeineddine HA, Girard R, Cao Y, Hobson N, Fam MD, Stadnik A, Tan H, Shen J, Chaudagar K, Shenkar R, et al. Quantitative susceptibility mapping as a monitoring biomarker in cerebral cavernous malformations with recent hemorrhage. J Magn Reson Imaging. 2018;47:1133–1138. doi: 10.1002/jmri.25831 [PubMed: 28791783]
23. Girard R, Li Y, Stadnik A, Shenkar R, Hobson N, Romanos S, Srinath A, Moore T, Lightle R, Shkoukani A, et al. A Roadmap for Developing Plasma Diagnostic and Prognostic Biomarkers of Cerebral Cavernous Angioma With Symptomatic Hemorrhage (CASH). Neurosurgery. 2021;88:686–697. doi: 10.1093/neuros/nyaa478 [PubMed: 33469662]
24. Sone JY, Hobson N, Srinath A, Romanos SG, Li Y, Carrion-Penagos J, Shkoukani A, Stadnik A, Piedad K, Lightle R, et al. Perfusion and Permeability MRI Predicts Future Cavernous Angioma Hemorrhage and Growth. J Magn Reson Imaging. 2022;55:1440–1449. doi: 10.1002/jmri.27935 [PubMed: 34558140]
25. Cardoso C, Arnould M, De Luca C, Otten C, Abdelilah-Seyfried S, Heredia A, Leutenegger AL, Schwaninger M, Tournier-Lasserve E, Boulday G. Novel Chronic Mouse Model of Cerebral Cavernous Malformations. Stroke. 2020;51:1272–1278. doi: 10.1161/STROKEAHA.119.027207 [PubMed: 31992178]
26. Detter MR, Shenkar R, Benavides CR, Neilson CA, Moore T, Lightle R, Hobson N, Shen L, Cao Y, Girard R, et al. Novel Murine Models of Cerebral Cavernous Malformations. Angiogenesis. 2020;23:651–666. doi: 10.1007/s10456-020-09736-8 [PubMed: 32710309]
27. DiStefano PV, Glading AJ. VEGF signalling enhances lesion burden in KRIT1 deficient mice. J Cell Mol Med. 2020;24:632–639. doi: 10.1111/jcmm.14773 [PubMed: 31746130]
28. Mleynek TM, Chan AC, Redd M, Gibson CC, Davis CT, Shi DS, Chen T, Carter KL, Ling J, Blanco R, et al. Lack of CCM1 induces hypersprouting and impairs response to flow. Hum Mol Genet. 2014;23:6223–6234. doi: 10.1093/hmg/ddu342 [PubMed: 24990152]
29. Gibson CC, Zhu W, Davis CT, Bowman-Kirigin JA, Chan AC, Ling J, Walker AE, Goitre L, Delle Monache S, Retta SF, et al. Strategy for identifying repurposed drugs for the treatment of cerebral cavernous malformation. Circulation. 2015;131:289–299. doi: 10.1161/CIRCULATIONAHA.114.010403 [PubMed: 25486933]

30. Hart BL, Taheri S, Rosenberg GA, Morrison LA. Dynamic contrast-enhanced MRI evaluation of cerebral cavernous malformations. Transl Stroke Res. 2013;4:500–506. doi: 10.1007/s12975-013-0285-y [PubMed: 24323376]

31. Claxton S, Kostourou V, Jadeja S, Chambon P, Hodivala-Dilke K, Fruttiger M. Efficient, inducible Cre-recombinase activation in vascular endothelium. Genesis. 2008;46:74–80. doi: 10.1002/dvg.20367 [PubMed: 18257043]

32. Fram EK, Herfkens RJ, Johnson GA, Glover GH, Karis JP, Shimakawa A, Perkins TG, Pelc NJ. Rapid Calculation of T1 Using Variable Flip Angle Gradient Refocused Imaging. Magn Reson Imaging. 1987;5:201–208. doi: Doi 10.1016/0730-725x(87)90021-X [PubMed: 3626789]

33. Mugler III JP, Kiefer B, Brookeman JR. Three-Dimensional T2-Weighted Imaging of the Brain Using Very Long Spin-Echo Trains. Paper/Poster presented Jan 01, 2000; Denver.

34. Mugler JP 3rd. Optimized three-dimensional fast-spin-echo MRI. J Magn Reson Imaging. 2014;39:745–767. doi: 10.1002/jmri.24542 [PubMed: 24399498]

35. Mugler JP 3rd, Bao S, Mulkern RV, Guttmann CR, Robertson RL, Jolesz FA, Brookeman JR. Optimized single-slab three-dimensional spin-echo MR imaging of the brain. Radiology. 2000;216:891–899. doi: 10.1148/radiology.216.3.r00au46891 [PubMed: 10966728]

36. Liang L, Korogi Y, Sugahara T, Shigematsu Y, Okuda T, Ikushima I, Takahashi M. Detection of intracranial hemorrhage with susceptibility-weighted MR sequences. AJNR Am J Neuroradiol. 1999;20:1527–1534. [PubMed: 10512241]

37. Wang KY, Idowu OR, Lin DDM. Radiology and imaging for cavernous malformations. Handb Clin Neurol. 2017;143:249–266. doi: 10.1016/B978-0-444-63640-9.00024-2 [PubMed: 28552147]

38. Labauge P, Laberge S, Brunereau L, Levy C, Tournier-Lasserve E. Hereditary cerebral cavernous angiomas: clinical and genetic features in 57 French families. Societe Francaise de Neurochirurgie. Lancet. 1998;352:1892–1897. doi: 10.1016/s0140-6736(98)03011-6 [PubMed: 9863787]

39. Rigamonti D, Hadley MN, Drayer BP, Johnson PC, Hoenig-Rigamonti K, Knight JT, Spetzler RF. Cerebral cavernous malformations. Incidence and familial occurrence. N Engl J Med. 1988;319:343–347. doi: 10.1056/NEJM198808113190605 [PubMed: 3393196]

40. Awad IA, Polster SP. Cavernous angiomas: deconstructing a neurosurgical disease. J Neurosurg. 2019;131:1–13. doi: 10.3171/2019.3.JNS181724 [PubMed: 31261134]

41. Flemming KD, Lanzino G. Cerebral Cavernous Malformation: What a Practicing Clinician Should Know. Mayo Clin Proc. 2020;95:2005–2020. doi: 10.1016/j.mayocp.2019.11.005 [PubMed: 32605781]

42. Greenberg SM, Vernooij MW, Cordonnier C, Viswanathan A, Al-Shahi Salman R, Warach S, Launer LJ, Van Buchem MA, Breteler MM, Microbleed Study G. Cerebral microbleeds: a guide to detection and interpretation. Lancet Neurol. 2009;8:165–174. doi: 10.1016/S1474-4422(09)70013-4 [PubMed: 19161908]

43. Hudnall R, Chen EX, Opperman PJ, Kelly S, Cramer JA, Surdell DL. A series of 14 representative presentations of cerebral cavernous malformations. Interdisciplinary Neurosurgery. 2021;26:101298. doi: 10.1016/j.inat.2021.101298

44. Tofts PS, Kermode AG. Measurement of the blood-brain barrier permeability and leakage space using dynamic MR imaging. 1. Fundamental concepts. Magn Reson Med. 1991;17:357–367. doi: 10.1002/mrm.1910170208 [PubMed: 2062210]

45. Hylton N Dynamic contrast-enhanced magnetic resonance imaging as an imaging biomarker. J Clin Oncol. 2006;24:3293–3298. doi: 10.1200/JCO.2006.06.8080 [PubMed: 16829653]

46. Labauge P, Denier C, Bergametti F, Tournier-Lasserve E. Genetics of cavernous angiomas. Lancet Neurol. 2007;6:237–244. doi: 10.1016/S1474-4422(07)70053-4 [PubMed: 17303530]

47. Morrison L, Akers A, Adam MP, Mirzaa GM, Pagon RA. Cerebral Cavernous Malformation, Familial. 2003:1993–2022.

48. Pozzati E, Acciarri N, Tognetti F, Marliani F, Giangaspero F. Growth, subsequent bleeding, and de novo appearance of cerebral cavernous angiomas. Neurosurgery. 1996;38:662–669; discussion 669–670. [PubMed: 8692382]

49. Shenkar R, Venkatasubramanian PN, Wyrwicz AM, Zhao JC, Shi C, Akers A, Marchuk DA, Awad IA. Advanced magnetic resonance imaging of cerebral cavernous malformations: part II.

Imaging of lesions in murine models. Neurosurgery. 2008;63:790–797; discussion 797–798. doi: 10.1227/01.NEU.0000315862.24920.49 [PubMed: 18981891]

50. Ridder DA, Lang MF, Salinin S, Roderer JP, Struss M, Maser-Gluth C, Schwaninger M. TAK1 in brain endothelial cells mediates fever and lethargy. J Exp Med. 2011;208:2615–2623. doi: 10.1084/jem.20110398 [PubMed: 22143887]
51. Lopez-Ramirez MA, Lai CC, Soliman SI, Hale P, Pham A, Estrada EJ, McCurdy S, Girard R, Verma R, Moore T, et al. Astrocytes propel neurovascular dysfunction during cerebral cavernous malformation lesion formation. J Clin Invest. 2021;131. doi: 10.1172/JCI139570

Highlights

- Chronic mouse model of cerebral cavernous malformations (CCM) has been created in the *Krit1* genetic background.
- Precise volumetric analysis of individual lesions has been performed for the first time, revealing complex progression trends.
- Modified dynamic contrast-enhanced (DCE) MRI indicated a high degree of heterogeneity in lesional permeability.
- Multivariate analysis of MRI properties and cellular markers revealed that increased cell density surrounding lesions correlates with stability, while increased vasculature within and surrounding lesions may correlate with instability.
- Some CCM patients have severe neurologic symptoms, while others remain asymptomatic; this marked phenotypic heterogeneity is puzzling. To address the clinical problem, we develop a sensitive pre-clinical CCM platform for testing of new imaging and therapeutic approaches.

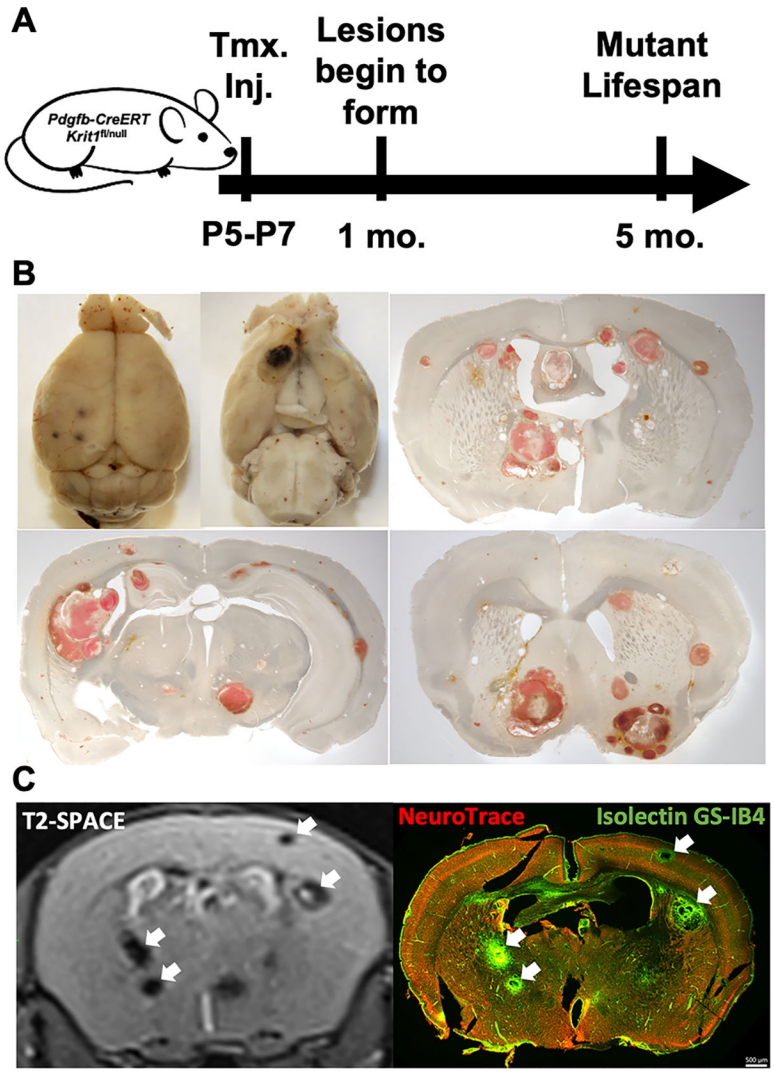

Figure 1. Induction of *Krit1* ablation at postnatal days 5–7 generates a chronic CCM murine model with gradual lesion development brain wide.

A, Timeline of chronic CCM model generation and disease phenotype. **B**, Macroscopic and brightfield images of lesion burden demonstrate that lesions form throughout the entire brain. **C**, Comparison of MRI (left) and fluorescence image (right) of the same CCM mouse brain section, demonstrating alignment of the corresponding lesions between the two imaging modalities. In the fluorescence image, lesions are stained with isolectin GS-IB4 (green) and neurons with NeuroTrace (red). Scale bar, 500 μm. White arrows denote lesions.

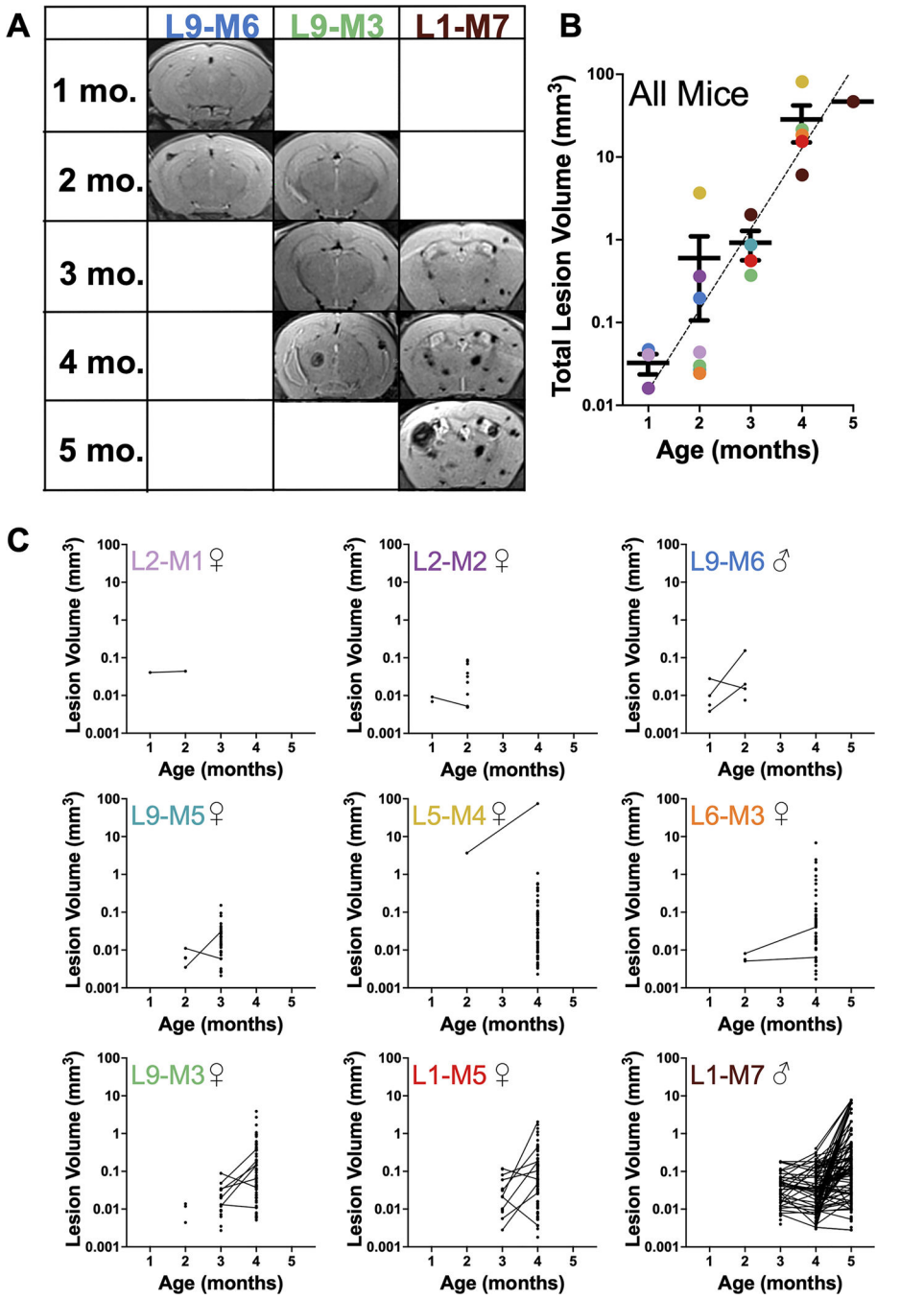

Figure 2. Volumetric analysis of lesions from longitudinal T2-SPACE MR images reveals dramatic increases in lesion burden with age and dynamic changes in size of individual lesions.

A, Representative T2-SPACE MR images from 3 mice in the cohort, illustrating formation of new lesions and dynamic changes in lesion size across time points. **B**, A semilogarithmic graph showing combined lesion volumes in each individual brain (n=9) as a function of age. Individual mice are represented with single-colored dots, corresponding with graph title colors in panel C. The trend line indicates the slope of the correlation (0.976±0.011 SEM, $p<0.001$) calculated with random coefficient regression analysis (Table S1). The bars

represent means±SEM. **C**, Semilogarithmic graphs of individual lesion volumes onto age for each mouse in the cohort. Lines connect lesions identified as corresponding lesions across imaging time points. Dots without connecting lines indicate de novo lesion formation or lesions that were only identified at a single time point. Graph titles indicate unique mouse ID where L# denotes litter number and M# denotes arbitrary mouse number within litter. Sex of mice is indicated with the symbol ♀ for females (n=7) and ♂ for males (n=2). Animated MRI sequences of L1-M7 are shown in Supplemental Videos S1–S3.

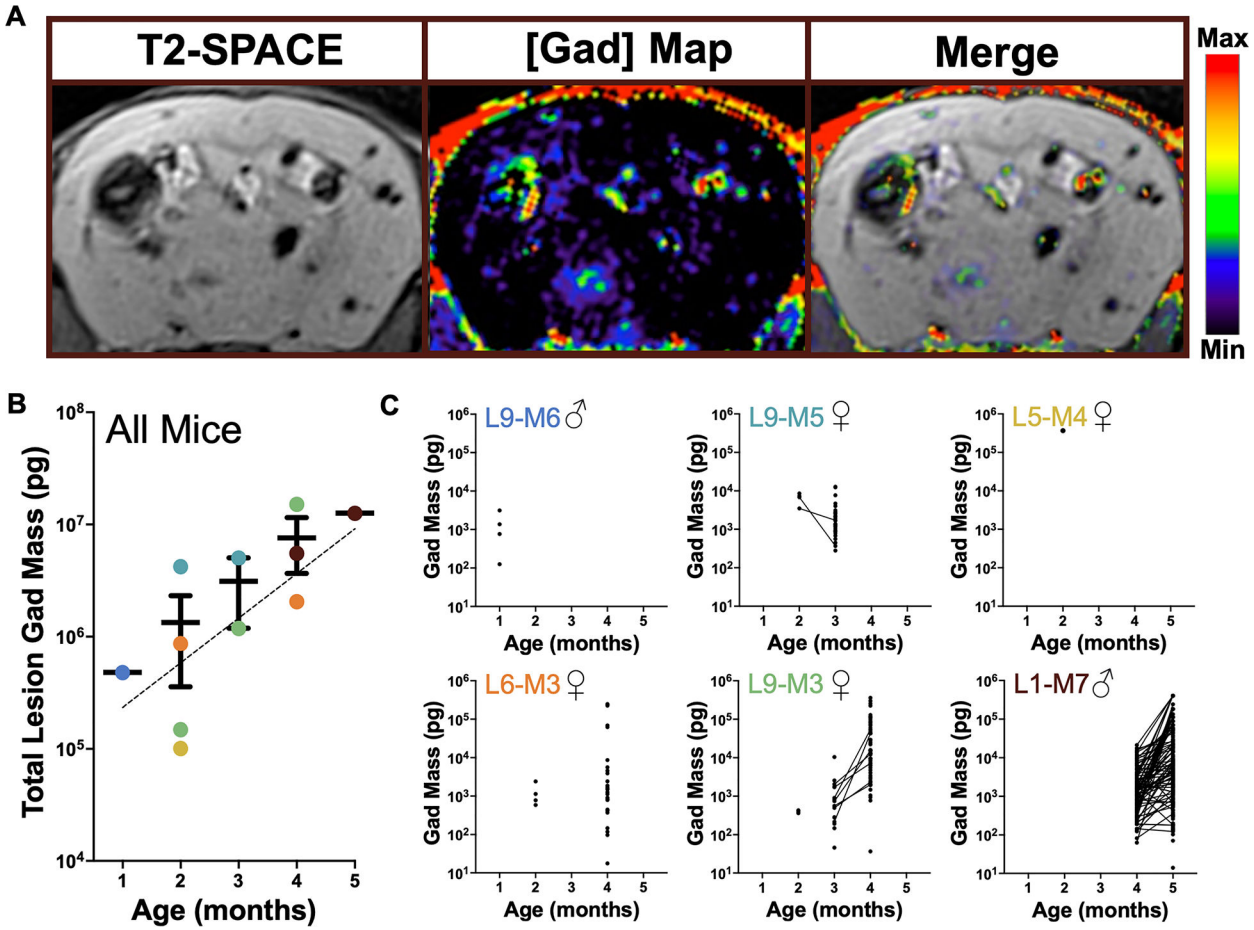

Figure 3. Lesion permeability analysis calculated from T1 contrast mapping reveals cumulative increase in gadolinium deposition with age.

A, Representative MR images of T2-SPACE, a corresponding gadolinium concentration plot generated with T1 contrast mapping, and a merged image, illustrating leakiness of individual lesions in terms of gadolinium deposition. In the gadolinium concentration map, hyperintense areas (red) indicate regions with higher gadolinium deposition. **B**, A semilogarithmic graph of combined lesional gadolinium mass in each brain (n=6) over age. Individual mice are represented as single-colored dots, corresponding with the color of graph titles in panel C. The trend line shows the slope of the correlation (0.398±0.089 SEM, p=0.004) calculated with random coefficient regression analysis (Table S2). The bars represent means±SEM. **C**, Semilogarithmic graphs of gadolinium deposition in individual lesions, as a function of age, for each individual mouse in the cohort. Lines connect lesions identified as matched lesion across the imaging time points. Dots without connecting lines indicate de novo lesion formation or lesions that were only identified at a single time point. Graph titles indicate unique mouse ID where L# denotes litter number and M# denotes arbitrary mouse number within litter. Sex of mice is indicated with the symbol ♀ for females (n=4) and ♂ for males (n=2). Animated MRI sequences of L1-M7 are shown in Supplemental Videos S1–S3.

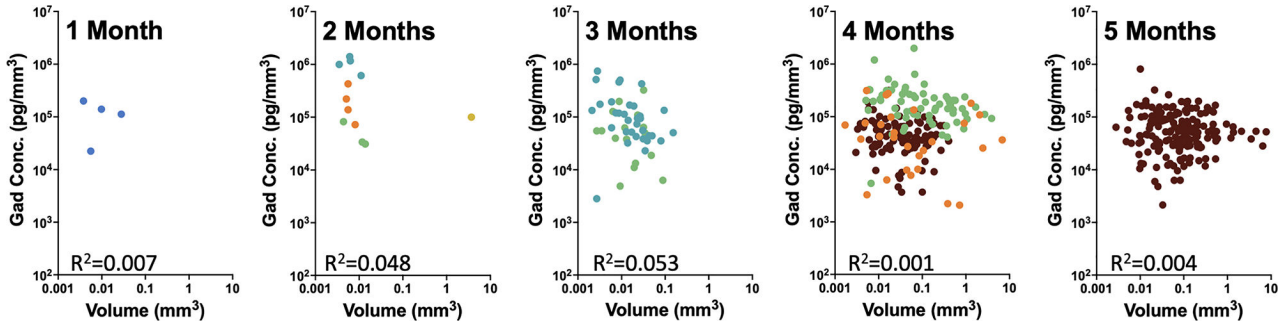

Figure 4. Lesion permeability displays a high degree of heterogeneity.

Log-log graphs of gadolinium concentration as a function of lesion volume for all individual lesions at each imaging timepoint. Individual mice (n=6) are represented with single-colored dots, which correspond with color-coding in Figures 2 and 3. The coefficient of determination (R^2) values indicate poor correlation between gadolinium concentration and volume for each time point, suggesting highly heterogenous permeability of lesions across age in the chronic *Krit1* CCM model.

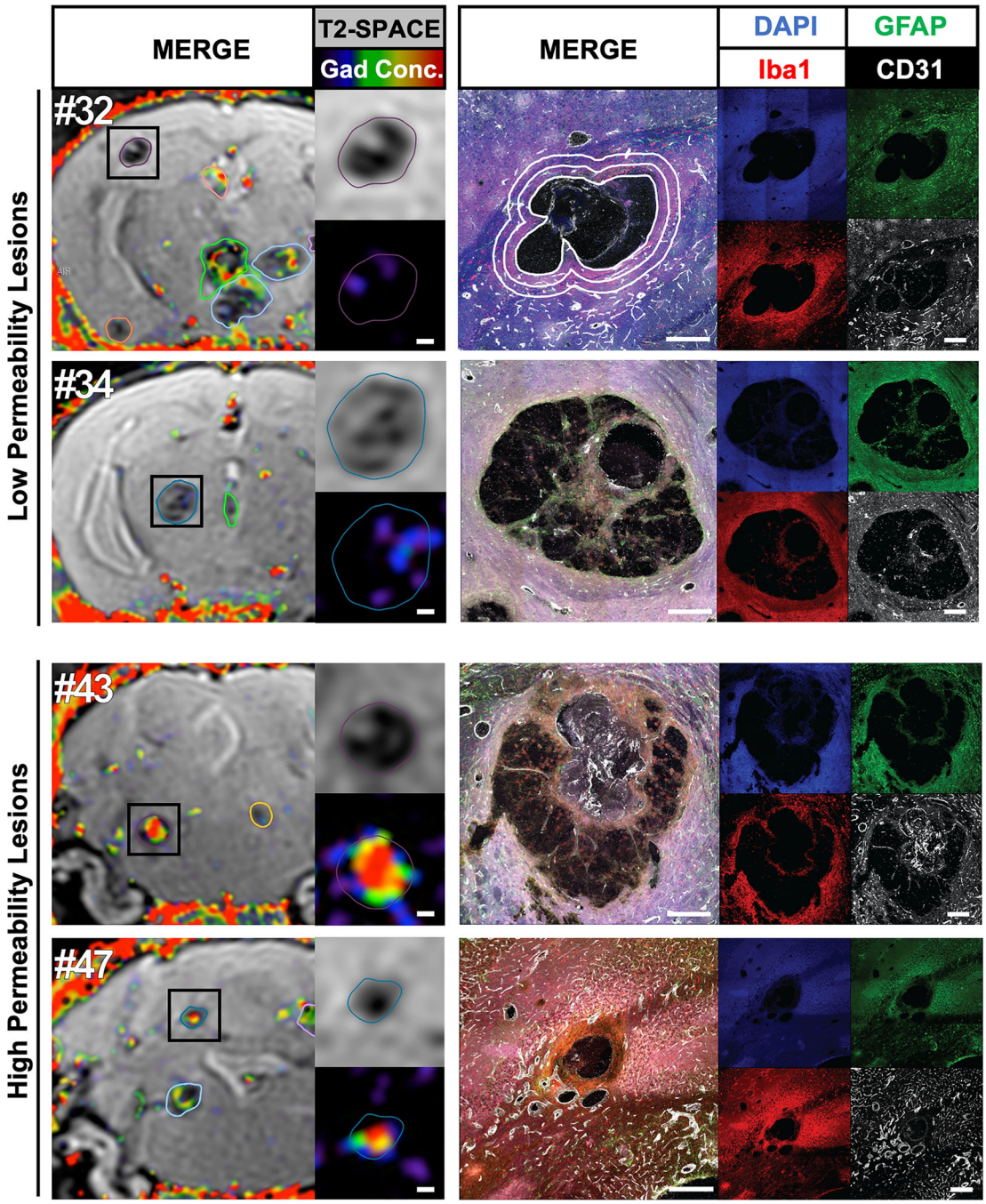

Figure 5. MRI and histochemical signatures of CCM lesions with low and high permeability in L9-M3 (n=1).

Two lesions with the lowest permeability (#32 in the subcortical corpus callosum, gadolinium concentration 41 ng/mm^3; and #34 in the thalamus, gadolinium concentration 58.9 ng/mm^3; Table S3) are shown on top. Two lesions with the highest permeability (#43 in the brainstem, gadolinium concentration 185.8 ng/mm^3; and #47 in the cerebellum, gadolinium concentration 250.5 ng/mm^3; see Table S3 for an overview of measurements) are shown at the bottom. MRI insets show T2-SPACE images and gadolinium concentration maps of each lesion in detail. Matching IHC images of each DAPI, GFAP, Iba1 and CD31

channels are shown on the right, next to the 4-channel overlay. Large, highly permeable lesions typically contain numerous CD31-positive endothelial cells. All scale bars are 200 μm. White lines drawn on the merged IHC image for lesion #32 exemplify the lesion border, 50 μm, and 100 μm perimeters used for correlation analysis. See Figure S7 for additional information.